Calculation of optical eigenmodes and gain in semipolar and nonpolar InGaN/GaN laser diodes

W. G. Scheibenzuber and U. T. Schwarz*
Institute of Experimental and Applied Physics, University of Regensburg, Universitätsstrasse 31, D-93053 Regensburg, Germany

R. G. Veprek and B. Witzigmann
Integrated Systems Laboratory, ETH Zurich, Gloriastrasse 35, CH-8092 Zurich, Switzerland

A. Hangleiter
Institute of Applied Physics, University of Braunschweig, Mendelssohnstrasse 2, D-38106 Braunschweig, Germany
(Received 22 April 2009; revised manuscript received 6 August 2009; published 21 September 2009)

We investigate the anisotropic optical gain in non-*c*-plane InGaN quantum wells with 20% indium content including band-gap renormalization and the screening of the quantum confined Stark effect. Waveguide modes and their polarizations are determined as TE and TM modes or extraordinary and ordinary modes, depending on the birefringence and the orientation of the laser diode's ridge waveguide relative to the *c* axis. The band structures and optical matrix elements along the polarization directions are calculated using a 6×6 $k\cdot p$ Hamiltonian and a self-consistent Schrödinger-Poisson solver. From these calculations the reduced density of states and the optical gain for the different polarizations are determined in the free-carrier picture with an *ad hoc* inclusion of the band-gap renormalization and compared to a *c*-plane quantum well. It is found that for high indium concentrations the gain can be significantly increased by going from the *c* plane to a semipolar or a nonpolar crystal orientation. However, due to birefringence and composition of the topmost valence-band wave function, the ridge has to be oriented along the $[\bar{1}\bar{1}23]$ direction for semipolar and along the [0001] direction for nonpolar laser diodes.

DOI: 10.1103/PhysRevB.80.115320 PACS number(s): 73.61.Ey, 42.55.Px, 78.66.Fd

I. INTRODUCTION

Violet and blue laser diodes made of InGaN show high output powers and low threshold currents, and so they are already commercially available in a range of applications. However, a green InGaN cw-laser diode, which would be desirable for applications such as laser projection, has not yet been realized. To date, the longest lasing wavelength which has been achieved with a *c*-plane InGaN laser diode is about 500 nm.[1] One main problem with green laser diodes is the quantum confined Stark effect (QCSE) due to the piezoelectric and spontaneous polarization in the quantum wells (QWs). It becomes stronger with rising indium content because of the strain that comes with the increased lattice mismatch. The QCSE draws the electron and the hole wave functions apart from each other, decreasing the wavefunction overlap and thus the optical matrix elements which enter the gain.[2] A possible solution to this problem is to reduce the QCSE by growing the laser diode on a different crystal plane than the *c* plane.[3] There have already been various publications demonstrating optically and electrically pumped light-emitting diode and laser structures on the $(11\bar{2}2)$ plane[4,5] and other semipolar and nonpolar planes,[6–8] even a fully functional nonpolar 499.8 nm diode laser[9] and a semipolar 531 nm diode laser[10] have recently been demonstrated. It is reported that these devices show a strong anisotropy in their optical properties, which can be explained by a microscopic analysis of the gain in semipolar and nonpolar quantum wells. The anisotropic properties of the band structure in non-*c*-plane quantum wells have already been investigated theoretically.[11,12] The present work analyzes the impact of the anisotropy on the optical eigenmodes and the gain in semipolar and nonpolar laser structures.

The semipolar crystal plane considered in this work is the $(11\bar{2}2)$ plane. Waveguides made of GaN alloys show uniaxial birefringence with $\Delta n=n_e-n_o\approx0.011n_o$,[13] with the extraordinary direction along the *c* axis of the wurtzite crystal. A $\lambda/2$ plate for 470 nm made of *a*-plane GaN would have to be about 9 μm thick, which is just a fraction of the length of common diode laser waveguides. In a birefringent semipolar waveguide, there are two principle directions that affect the polarization of the optical eigenmodes: the *c* axis of the wurtzite crystal and the growth axis of the waveguide. Two possible structures have to be distinguished: the ridge waveguide can be oriented either parallel or perpendicular to the projection of the *c* axis in the QW plane (see Fig. 1), pointing along the $[\bar{1}\bar{1}23]$ or the $[1\bar{1}00]$ direction, respectively. For the first possibility, the ordinary and the extraordinary directions perpendicular to the propagation direction match the TM- and the TE-polarization directions and so TE and TM modes exist, with polarizations perpendicular and parallel to the growth axis, respectively. For ridge waveguides on semipolar substrates with a ridge orientation parallel to the projection of the *c* axis, laser facets have to be formed by etching.[6] The alternative direction offers the possibility to cleave facets, but the extraordinary direction is then rotated in a plane perpendicular to the propagation direction, causing optical modes different from TE and TM, with polarizations parallel and perpendicular to the *c* axis. The shapes and polarizations of these modes are calculated in this work using a 4×4 transfer-matrix method from[14] which is described in Appendix A. Polarizations have to be considered when calculating the optical gain, as they determine the direction of the relevant momentum matrix elements. It has to be pointed out that a calculation of TE and

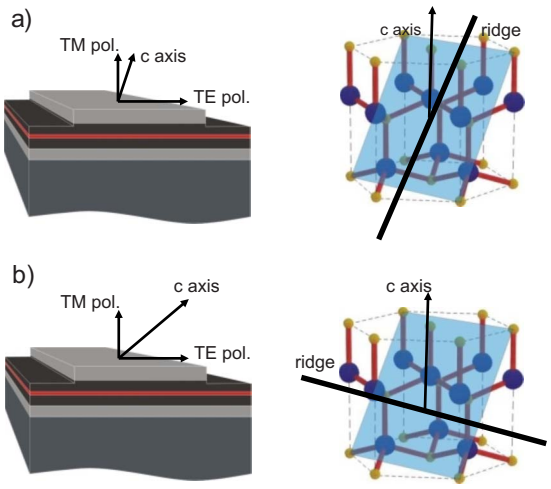

FIG. 1. (Color online) Ridge geometries and crystal orientations of two possible realizations of a laser structure on the $(11\bar{2}2)$ plane (indicated by the transparent plane on the crystal images). (a) ridge along $[\bar{1}\bar{1}23]$ and (b) ridge along $[1\bar{1}00]$.

TM optical gain does not make sense in a laser diode structure that does not show TE and TM modes, and we show later in this work (see Sec. III C) why a projection of TE and TM optical gain on the photon polarization direction is not correct.

As a consequence of using a semipolar or a nonpolar substrate, the band structure does no longer have rotational symmetry in the QW plane, so all relevant quantities depend on both the wave number k' and the in-plane angle $\phi = \arctan(k'_y/k'_x)$ of electrons and holes. It is thus necessary for determining the gain to integrate over k' and ϕ, which adds considerable numerical effort to the calculation.

II. EIGENMODES OF A BIREFRINGENT WAVEGUIDE

In a *c*-plane laser diode, the extraordinary direction is perpendicular to the growth plane. The eigenmodes of the electric field in these diodes are called TE or TM, with polarization perpendicular or along the *c* axis, respectively. However, if a waveguide structure is grown on a different plane of the wurtzite crystal and a ridge is formed perpendicular to the extraordinary direction, then there is a competition between the transversal refractive index profile, which favors polarizations parallel or perpendicular to the growth plane, and the optical anisotropy, which pulls the polarization of the modes into the ordinary and the extraordinary directions intrinsic to the crystal. This is the case for the ridge orientation along the $[1\bar{1}00]$ direction, which is treated in this section. The eigenmodes of such a birefringent waveguide were called "supermodes" in Ref. 14. However, it appears that this term is also used for arrays of phase-locked filaments,[15] so we avoid it here.

A. Laser diode structure

Figure 2 shows the structure of the waveguide, which is formed by a 200 nm thin GaN film with GaN/InGaN active zone and AlGaN electron blocking layer between two AlGaN cladding layers, and the coordinate system for the waveguide. Table I contains the thicknesses of the individual layers of the simulated diode structure. To reduce the numerical effort, the active layer with three InGaN QWs and GaN spacing layers is treated as one layer with averaged refractive index. The thickness of the three quantum wells is 3 nm and the spacing between them is 7 nm. The z' axis points along the growth direction and the wave propagates along the y' direction. In the x'-z' plane lies the *c* axis, which is tilted by the crystal angle $\theta = 58°$ with respect to the growth direction, so the waveguide plane corresponds to the $(11\bar{2}2)$ crystal plane. The film extends to infinity in the x'-y' plane. Primed coordinates are used here because the unprimed ones will be used for the crystal directions in the description of the quantum well (Sec. III). We emphasize that the detailed structure of the laser diode is uncritical. Even a single 200 nm GaN waveguide shows the discussed effect. The dielectric tensor ε for this structure is obtained by rotating the dielectric tensor of a *c*-plane structure by the crystal angle $\theta = 58°$ around the y' axis as follows:

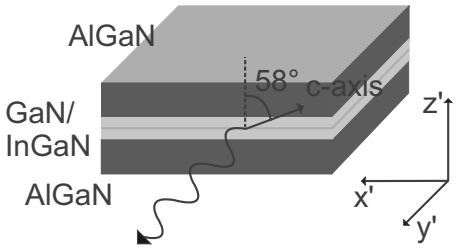

FIG. 2. Waveguide structure with coordinate system.

$$\varepsilon = U^T \begin{pmatrix} n_o^2 & 0 & 0 \\ 0 & n_o^2 & 0 \\ 0 & 0 & n_e^2 \end{pmatrix} U,$$

$$U = \begin{pmatrix} \cos(\theta) & 0 & \sin(\theta) \\ 0 & 1 & 0 \\ -\sin(\theta) & 0 & \cos(\theta) \end{pmatrix}. \quad (1)$$

TABLE I. Layer thicknesses and materials for the simulated diode structure.

Layer	Material	Thickness (nm)
p cladding	$Al_{0.05}Ga_{0.95}N$	600
p waveguide	GaN	50
Electron blocker	$Al_{0.2}Ga_{0.8}N$	5
Spacer	GaN	25
Active layer	$GaN/In_{0.2}Ga_{0.8}N$	30
n waveguide	GaN	90
n cladding	$Al_{0.05}Ga_{0.95}N$	1000

TABLE II. Refractive indices of the materials used in the calculation.

Material	n_o	n_e
$Al_{0.05}Ga_{0.95}N$	2.424	2.461
$Al_{0.2}Ga_{0.8}N$	2.341	2.376
GaN	2.454	2.481
$In_{0.2}Ga_{0.8}N$	2.821	2.883

B. Refractive indices

For the simulation one needs both the ordinary and the extraordinary refractive indices of the considered materials at the desired wavelength. Refractive index data for GaN films on different substrates are available from experiments using spectroscopic ellipsometry[13] and polarized reflectance spectroscopy.[16] In Refs. 17 and 18, a prism coupling method and spectroscopic transmittance and reflectance measurements were used to obtain refractive indices of the alloys AlGaN with Al contents of 0, 0.144, and 0.234 (higher Al contents are not relevant for this work) and InGaN with an In content of ≤ 0.1.

Although fits to the experimental values for a limited range of wavelengths were provided for the GaN and the AlGaN data, they are not sufficient to describe the desired waveguide structure, as values were given only for a few alloy compositions without a rule to interpolate between them. Instead, a theoretical model for AlGaN and InGaN alloys for the ordinary refractive index from Ref. 19 is used for the simulation. The optical anisotropy is taken into account by using the relative anisotropy $\Delta n/n_o$ of the materials from the mentioned references for the alloys. Table II shows the values that are used for the refractive indices.

C. Eigenmodes and polarizations

Waveguide modes are calculated using the method described in Appendix A for a wavelength of 470 nm. The results for the fundamental mode (the one with the highest effective index of refraction) and the first mode perpendicular to the fundamental one are shown in Figs. 3 and 4. It is found that the eigenmodes of this anisotropic waveguide are not TE and TM modes polarized in the x' and the z' directions, respectively, like in the nonbirefringent case. Instead, their average polarization approximately points along the ordinary or the extraordinary direction of the crystal in the x'-z' plane, so in the following they will be called extraordinary and ordinary modes. The effective indices of refraction for these two modes are $n_{\text{eff}}=2.466$ for the extraordinary and $n_{\text{eff}}=2.432$ for the ordinary mode. In both cases the x' and the z' components are real valued functions, so the modes are linearly polarized. Small discontinuities in the z' component at the borders of the GaN layer lead to a step in the angle $\alpha'=\arctan(E_{x'}/E_{z'})$. The polarization of the mode is nearly aligned to the ordinary or the extraordinary direction in the waveguide layer with a maximum deviation of about 2°. Furthermore, there is a small longitudinal component $E_{y'}$ which is imaginary.

The most important is the polarization angle inside the active region, which deviates by some degrees from the crystal directions, depending on the thicknesses of the layers. However, in order to get a description that is independent of the specific form of the waveguide, we use the ordinary and the extraordinary directions as mode polarizations in our gain calculation, which is an acceptable approximation.

D. Variation of the anisotropy

It has already been pointed out in Ref. 14 that if the symmetry of the dielectric tensor is different from the symmetry prescribed by the growth of the epitaxial layers, then new eigenmodes are established which are tilted with respect to the TE and TM orientation. This tilt is determined by the strength and orientation of the anisotropy. Such a behavior has been measured for ordered GaInP/AlGaInP quantum well structures in Ref. 20. In that case, birefringence was induced by ordering effects and $\Delta n/n_o$ was smaller than 0.003. For AlGaN/GaN waveguides the relative anisotropy is higher, about $\Delta n/n_o=0.011$, which almost completely pulls the modes into the ordinary and the extraordinary directions.

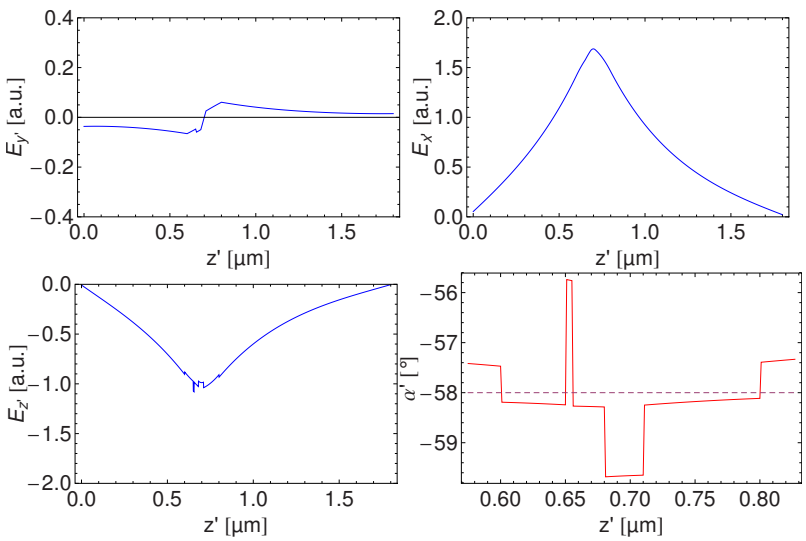

FIG. 3. (Color online) Electric field components of the extraordinary mode of the semipolar waveguide and angle $\alpha'=\arctan(E_{x'}/E_{z'})$ as a function of z' near the waveguide layer (y' component divided by the complex unit). The dashed line indicates the extraordinary direction.

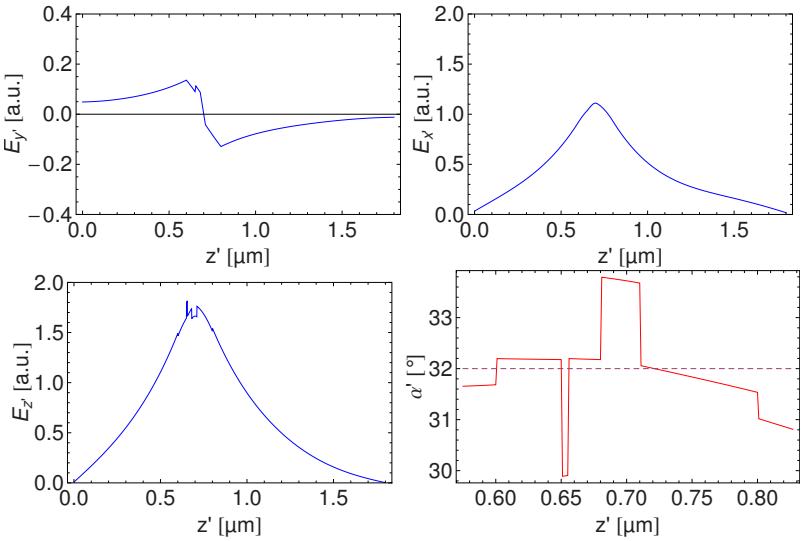

FIG. 4. (Color online) Electric field components of the ordinary mode of the semipolar waveguide and angle α' as a function of z' near the waveguide layer (y' component divided by the complex unit). The dashed line indicates the ordinary direction.

In order to see the influence of the strength of the anisotropy, a factor ξ is introduced in the calculation, which illustrates the transition from isotropic ($\xi=0$) to strong anisotropic behavior ($\xi=1$). In this calculation, only a GaN waveguide without an electron blocking layer and an active region is considered to reduce the numerical effort. The extraordinary refractive indices are set to $\xi n_e+(1-\xi)n_o$. Figure 5 shows the average angle

$$\alpha'_{avg} = \int dz'\ \vec{E}(z')^2\alpha'(z')/[\int dz'\ \vec{E}(z')^2]$$

of the mode as a function of ξ for two different waveguide thicknesses. A transition from TE and TM modes to extraordinary and ordinary modes takes place in the range of $\xi=0$ to $\xi=0.2$. This means that, already at 20% of the anisotropy of GaN, the modes point almost exactly along the crystal directions. If the waveguide layer's thickness is changed to 100 nm, the pull into the crystal directions is even stronger. Note that in the bulk case (layer thickness of 0 or ∞), the modes point exactly along the crystal directions for arbitrarily weak anisotropy, as these are the only specified directions in the absence of a layer border.

III. GAIN CALCULATION

In order to calculate the gain of a semipolar quantum well, one has to determine the band structure, the electron and hole wave functions depending on the in-plane wave vector, and the band-gap renormalization for different charge-carrier densities. To do so we use a 6×6 $k\cdot p$ valence-band Hamiltonian and we solve the Schrödinger and Poisson equations self-consistently to account for the screening of the QCSE by the charge carriers.

A. Coordinate systems

Our description of the semipolar quantum well follows the notation of Ref. 12: primed coordinates correspond to the directions in the quantum well coordinate system, while unprimed ones correspond to the crystal directions. So x' and y' are in the QW plane, z' points along the growth direction, whereas z points along the c axis and x,y point along the $[11\bar{2}0]$ and the $[1\bar{1}00]$ directions, respectively (see Fig. 6). The y axis is chosen as the rotation axis to obtain a description for the semipolar and nonpolar planes. For the $(11\bar{2}2)$ plane the crystal angle (the angle between the c axis and the growth direction) is $\theta=58°$. Setting $\theta=90°$ corresponds to the nonpolar $(11\bar{2}0)$ a plane. The unprimed coordinates are then related to the primed ones via the rotation matrix from Eq. (1),

$$\begin{pmatrix} x \\ y \\ z \end{pmatrix} = U \begin{pmatrix} x' \\ y' \\ z' \end{pmatrix}. \tag{2}$$

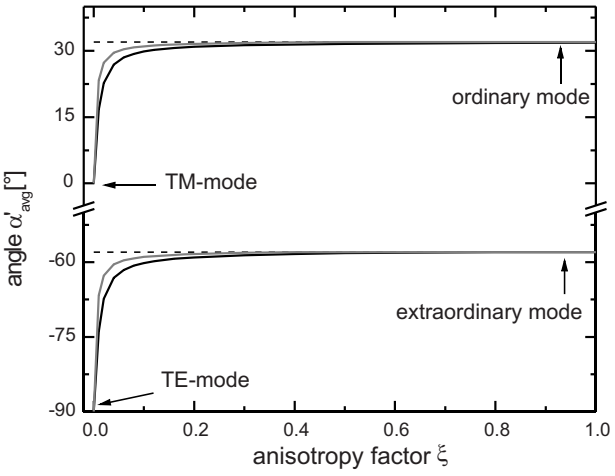

FIG. 5. Average angle α'_{avg} of both modes as a function of the anisotropy factor for a waveguide thickness of 200 nm (black lines) and 100 nm (gray lines)

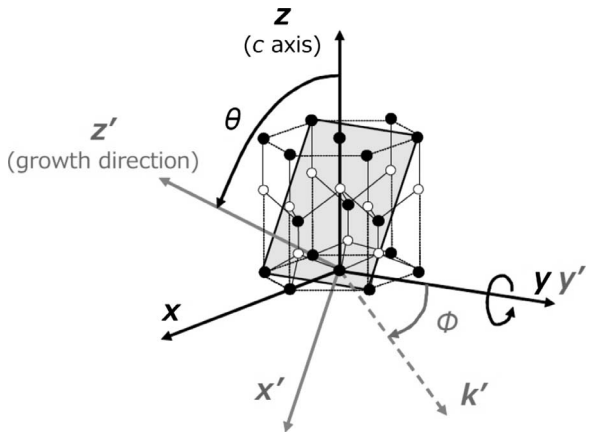

FIG. 6. Definition of crystal angle and coordinates (Ref. 12).

B. Valence-band and conduction-band Hamiltonian

The band structure of an InGaN crystal in the vicinity of the Γ point can be described by a $k\cdot p$ ansatz using the following six basis states:

$$|U_1\rangle = -\frac{1}{\sqrt{2}}(|P_x\uparrow\rangle + i|P_y\uparrow\rangle),$$

$$|U_2\rangle = \frac{1}{\sqrt{2}}(|P_x\uparrow\rangle - i|P_y\uparrow\rangle),$$

$$|U_3\rangle = |P_z\uparrow\rangle,$$

$$|U_4\rangle = \frac{1}{\sqrt{2}}(|P_x\downarrow\rangle - i|P_y\downarrow\rangle),$$

$$|U_5\rangle = -\frac{1}{\sqrt{2}}(|P_x\downarrow\rangle + i|P_y\downarrow\rangle),$$

$$|U_6\rangle = |P_z\downarrow\rangle.$$

The 6×6 valence-band Hamiltonian for the bulk crystal is then[21,22]

$$\mathbf{H_v}(k_x,k_y,k_z) = \begin{pmatrix} F & -K^* & -H^* & 0 & 0 & 0 \\ -K & G & H & 0 & 0 & \Delta \\ -H & H^* & \Lambda & 0 & \Delta & 0 \\ 0 & 0 & 0 & F & -K & H \\ 0 & 0 & \Delta & -K^* & G & -H^* \\ 0 & \Delta & 0 & H^* & -H & \Lambda \end{pmatrix}, \tag{3}$$

where

$$F = \Delta_{cr} + \frac{\Delta_{so}}{3} + \Lambda + \Theta,$$

$$G = \Delta_{cr} - \frac{\Delta_{so}}{3} + \Lambda + \Theta,$$

$$\Lambda = \frac{\hbar^2}{2m_0}[A_1 k_z^2 + A_2(k_x^2 + k_y^2)] + \Lambda_\epsilon,$$

$$\Theta = \frac{\hbar^2}{2m_0}[A_3 k_z^2 + A_4(k_x^2 + k_y^2)] + \Theta_\epsilon,$$

$$K = \frac{\hbar^2}{2m_0}A_5(k_x + ik_y)^2 + D_5(\epsilon_{xx} - \epsilon_{yy}),$$

$$H = \frac{\hbar^2}{2m_0}A_6(k_x + ik_y)k_z + D_6\epsilon_{xz},$$

$$\Lambda_\epsilon = D_1\epsilon_{zz} + D_2(\epsilon_{xx} + \epsilon_{yy}),$$

$$\Theta_\epsilon = D_3\epsilon_{zz} + D_4(\epsilon_{xx} + \epsilon_{yy}),$$

$$\Delta = \frac{\sqrt{2}}{3}\Delta_{so}.$$

The valence-band effective-mass parameters A_i, the deformation potentials D_i ($i=1-6$), the splitting energies Δ_{cr} and Δ_{so}, and all other physical parameters appearing in the following are taken from Ref. 22. The strain coefficients ϵ_{ij} are calculated from a model given in Ref. 3

$$\epsilon_{xx} = \epsilon_{xx}^{(0)} + \epsilon_{xz}\tan\theta, \tag{4}$$

$$\epsilon_{yy} = \epsilon_{xx}^{(0)}, \tag{5}$$

$$\epsilon_{zz} = \epsilon_{zz}^{(0)} + \epsilon_{xz}\cot\theta, \tag{6}$$

$$\epsilon_{xz} = -\frac{\{[c_{11}\epsilon_{xx}^{(0)} + c_{12}\epsilon_{xx}^{(0)} + c_{13}\epsilon_{zz}^{(0)}]\sin^2\theta + [2c_{13}\epsilon_{xx}^{(0)} + c_{33}\epsilon_{zz}^{(0)}]\cos^2\theta\}\cos\theta\sin\theta}{c_{11}\sin^4\theta + 2(c_{13} + 2c_{44})\sin^2\theta\cos^2\theta + c_{33}\cos^4\theta}, \tag{7}$$

with $\epsilon_{xx}^{(0)}=(a_s-a_e)/a_e$ and $\epsilon_{zz}^{(0)}=(c_s-c_e)/c_e$. All other strain coefficients are zero and thus they are omitted in the Hamiltonian. a_s, c_s, a_e, c_e are the lattice constants of the substrate and the quantum well, respectively, and c_{ij} are the elastic constants of $In_{0.2}Ga_{0.8}N$. For the conduction band, the basis states are $|S\uparrow\rangle$ and $|S\downarrow\rangle$ and the bulk Hamiltonian has the form[22]

$$\mathbf{H_c}(k_x,k_y,k_z) = E_c + \frac{\hbar^2(k_x^2+k_y^2)}{2m_\parallel} + \frac{\hbar^2 k_z^2}{2m_\perp} + a_{c1}\epsilon_{zz} + a_{c2}(\epsilon_{xx}+\epsilon_{yy}), \tag{8}$$

where

$$E_c = E_g + \Delta_{cr} + \Delta_{so}/3,$$

$$a_{c1} = a_1 + D_1,$$

$$a_{c2} = a_2 + D_2.$$

In order to describe a non-c-plane quantum well, we have to go from the unprimed to the primed coordinates by inserting the vector $\vec{k}'$ rotated with the matrix U from Eq. (1) for $\vec{k}$ into both Hamiltonians. Furthermore, we consider quantum confinement in the envelope approximation[23] by adding a rectangular potential $V_{QW,v/c}(z')$ and substituting k_z' by $-i\frac{d}{dz'}$. The band offset ratio $\Delta E_v/\Delta E_c$ is taken as 0.2/0.8 from Ref. 24. Finally, the electric potential $\Phi_p(z')$ that is generated by the piezoelectric and spontaneous polarization must also be considered. With these additional terms, the Schrödinger equations for valence- and conduction-band electrons are

$$\left[\mathbf{H_v}\left(\frac{d}{dz'}\right) + V_v(z')\right]\vec{\psi}_v^{(n)}(z') = E_v^{(n)}\vec{\psi}_v^{(n)}(z'), \tag{9}$$

$$\left[\mathbf{H_c}\left(\frac{d}{dz'}\right) + V_c(z')\right]\psi_c^{(n)}(z') = E_c^{(n)}\psi_c^{(n)}(z'), \tag{10}$$

with $V_{v/c}(z')=V_{QW,v/c}(z')+\Phi_p(z')$.

Here, $\vec{\psi}_v^{(n)}(z')$ is a vector function whose components are the coefficients of the six valence-band basis states and n is the subband index

$$\vec{\psi}_v^{(n)}(z') \triangleq \psi_{v,1}^{(n)}(z')\left(-\frac{1}{\sqrt{2}}(|P_x\uparrow\rangle + i|P_y\uparrow\rangle)\right) + \psi_{v,2}^{(n)}(z') \times\left(\frac{1}{\sqrt{2}}(|P_x\uparrow\rangle - i|P_y\uparrow\rangle)\right) + \cdots + \psi_{v,6}^{(n)}(z')|P_z\downarrow\rangle. \tag{11}$$

The conduction band is spin degenerate, so the scalar wave function $\psi_c^{(n)}(z')$ is the same for spins up and down. Both wave functions also depend on the wave number k' and the in-plane angle $\phi=\arctan(k_y'/k_x')$, but these additional indices have been omitted to simplify the notation. These Schrödinger equations are solved numerically using a Fourier expansion method described in Appendix B. Figure 7 shows calculated band structures for the topmost valence bands in a 3 nm $In_{0.2}Ga_{0.8}N$ quantum well with c-plane, semipolar $(11\bar{2}2)$, and nonpolar $(11\bar{2}0)$ crystal orientations.

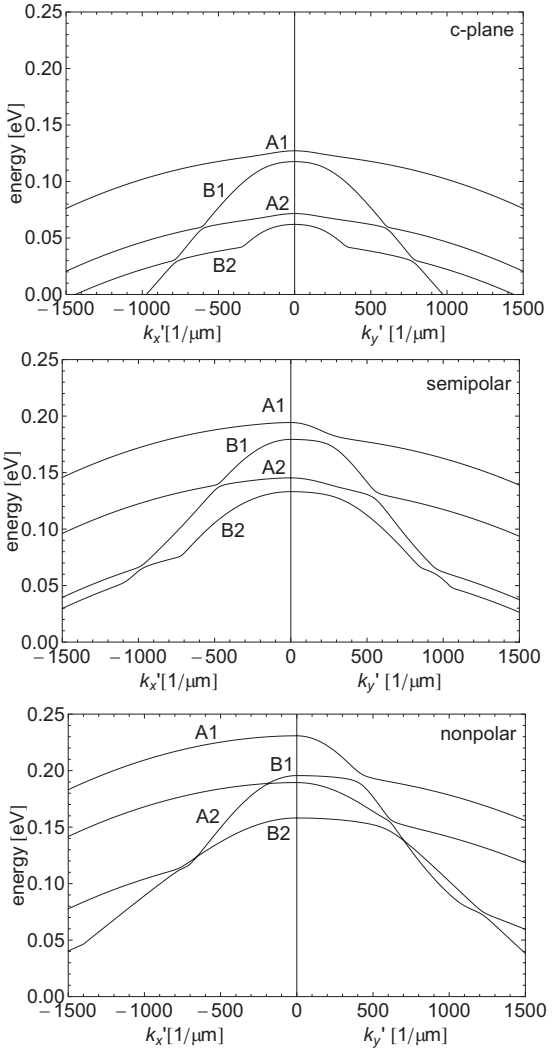

FIG. 7. Topmost valence bands in a 3 nm $In_{0.2}Ga_{0.8}N$ quantum well for different crystal orientations at a sheet-carrier density of 7×10^{12} cm^{-2}. Subbands that correspond to different bulk valence bands have been labeled A and B.

It becomes clear that for a non-c-plane crystal orientation the in-plane energy dispersion relation is anisotropic. To calculate the gain, it is thus necessary to know the band structure not only along two directions, but for the whole k_x', k_y' plane. Examples for the in-plane energy dispersion relation of the valence subbands can be seen in Fig. 8.

C. Transition matrix element

As mentioned before, it is possible to create ridge waveguides on semipolar crystal planes that do not show TE and TM modes due to the optical anisotropy. To see how this anisotropy enters the gain calculation, one has to take a look at the derivation of the transition matrix element. The general Hamiltonian (without $k\cdot p$ approximation) for a semiconductor in a monochromatic electric field is

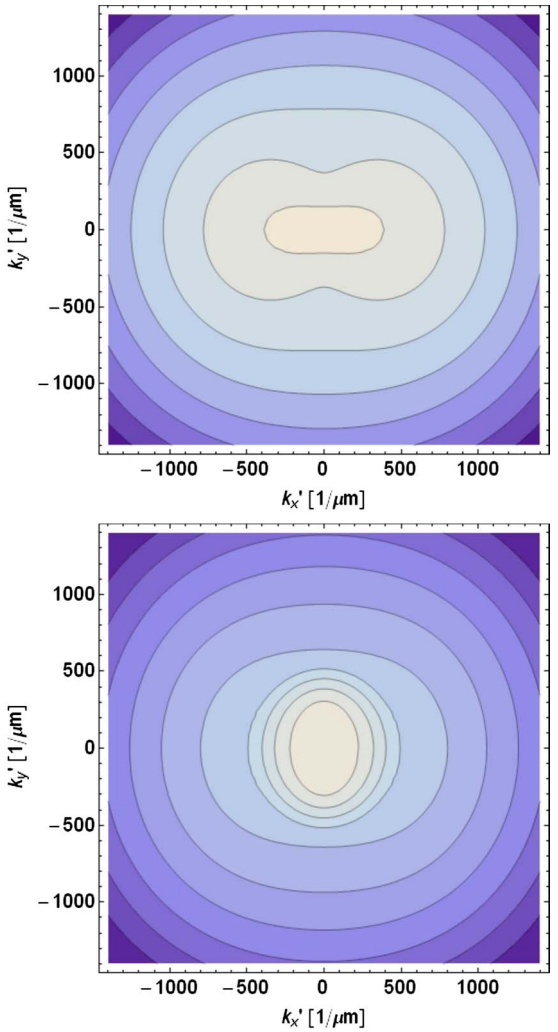

FIG. 8. (Color online) In-plane energy dispersion relation for valence subbands A1 (top) and B1 (bottom) in a semipolar 3 nm $In_{0.2}Ga_{0.8}N$ quantum well at a sheet-carrier density of 7×10^{12} cm^{-2}. The energy spacing is 10 meV per solid line.

$$H = \frac{(\vec{p} - e\vec{A})^2}{2m_0} + V_{\text{crystal}} + V_{QW} + \Phi_p$$
$$= \underbrace{\frac{\vec{p}^2}{2m_0} + V_{\text{crystal}} + V_{QW} + \Phi_p}_{H_o}$$
$$\underbrace{-\frac{e}{2m_0}(\vec{A}\cdot\vec{p} + \vec{p}\cdot\vec{A})}_{H_{\text{int}}} + \underbrace{o(\vec{A}^2)}_{\text{omitted}}. \tag{12}$$

Here, V_{crystal} is the periodic crystal potential, V_{QW} is the step potential of the quantum well, and Φ_p is the static electric potential. The terms labeled with H_0 are approximated by our $k\cdot p$ Hamiltonian, the interaction term H_{int} is treated as a perturbation, and the $\vec{A}^2$ term is omitted as usual. For the gain calculation, we need to find a simple expression for the transition matrix elements $\langle i|H_{\text{int}}|f\rangle$. First of all, the vector potential $\vec{A}$ can be expressed in terms of the electric field. In an appropriate gauge we have $\vec{E} = -\frac{\partial}{\partial t}\vec{A}$,

$$\vec{E}(\vec{r},t) = \sum_m \vec{\mathcal{E}}^{(m)*}(\vec{r})e^{i\omega t} + \vec{\mathcal{E}}^{(m)}(\vec{r})e^{-i\omega t},$$

$$\vec{A}(\vec{r},t) = \sum_m \frac{1}{i\omega}(\vec{\mathcal{E}}^{(m)}(\vec{r})e^{-i\omega t} - \vec{\mathcal{E}}^{(m)*}(\vec{r})e^{i\omega t}), \tag{13}$$

where we have used that the electric field is monochromatic and a superposition of eigenmodes that evolve with $e^{\pm i\omega t}$. It can be seen from Eq. (13) that the interaction Hamiltonian decomposes to separate terms for each mode. We can thus reduce our notification to one mode, omitting the mode index m from now on. Let N_{ph} be the number of photons in the mode, then the normalization of the mode function is found by the condition

$$\hbar\omega N_{ph} = \frac{1}{2}\int d^3r\varepsilon_0\vec{E}(\vec{r},t)\cdot\varepsilon(\vec{r})\cdot\vec{E}(\vec{r},t) + \frac{1}{2}\int d^3r\frac{1}{\mu_0}\vec{B}^2(\vec{r},t). \tag{14}$$

The time dependence of the energy in Eq. (14) must vanish and if we assume that the time average of the magnetic energy is the same as the electric energy, we can simplify the integral on the right-hand side to

$$\hbar\omega N_{ph} = \left\langle \int d^3r\varepsilon_0\vec{E}(\vec{r},t)\cdot\varepsilon(\vec{r})\cdot\vec{E}(\vec{r},t)\right\rangle_T$$
$$= 2\int d^3r\varepsilon_0\Re[\vec{\mathcal{E}}^*(\vec{r})\cdot\varepsilon(\vec{r})\cdot\vec{\mathcal{E}}(\vec{r})]$$
$$\approx 2\varepsilon_0 n_{eff}^2\int d^3r|\vec{\mathcal{E}}(\vec{r})|^2, \tag{15}$$

where $\langle\cdots\rangle_T$ denotes the time average and the dielectric tensor is approximated by the effective index of refraction n_{eff}^2. The next step is to introduce the dipole approximation, neglecting the spatial dependence of the vector potential in the quantum well region. Therefore, the intensity inside the quantum well is averaged as

$$|\vec{\mathcal{E}}_{avg}|^2 = \frac{1}{Ad}\int_{QW} d^3r|\vec{\mathcal{E}}(\vec{r})|^2 = \frac{1}{Ad}\Gamma\frac{\hbar\omega N_{ph}}{2\varepsilon_0 n_{eff}^2} \tag{16}$$

with the area A and thickness d of the quantum well and the confinement factor

$$\Gamma = \frac{\int_{QW} d^3r|\vec{\mathcal{E}}(\vec{r})|^2}{\int d^3r|\vec{\mathcal{E}}(\vec{r})|^2}. \tag{17}$$

The average value of the mode function in the quantum well is then given as

$$\vec{\mathcal{E}}_{avg} = \vec{a}\sqrt{\frac{1}{Ad}\Gamma\frac{\hbar\omega N_{ph}}{2\varepsilon_0 n_{eff}^2}}. \tag{18}$$

Here, $\vec{a}$ is a unit vector pointing along the average polarization direction of the mode in the quantum well. Inserting this result for the electric field into the vector potential yields the following expression for the interaction Hamiltonian:

$$H_{\text{int}} = \frac{e}{m_0}(\vec{a}\cdot\vec{p})\sqrt{\frac{1}{Ad}\Gamma\frac{\hbar\omega N_{ph}}{2\varepsilon_0 n_{eff}^2}}\frac{1}{i\omega}(e^{i\omega t} - e^{-i\omega t}). \quad (19)$$

The two terms of this interaction Hamiltonian correspond to the stimulated emission and the absorption. Finally, the transition matrix element for the stimulated emission is

$$|\langle i|H_{\text{int}}^{SE}|f\rangle|^2 = \frac{e^2}{m_0^2}|\langle i|\vec{a}\cdot\vec{p}|f\rangle|^2\Gamma\frac{1}{Ad}\frac{\hbar N_{ph}}{2\varepsilon_0 n_{eff}^2\omega}. \quad (20)$$

It can be seen from this expression that the momentum matrix elements have to be oriented along the polarization direction of the mode. Using this transition matrix element, one can calculate the modal gain for a specific quantum well and waveguide structure. If one is interested in the material gain for a quantum well, one can divide the transition matrix element by the confinement factor, as modal and material gain are related to each other via

$$G^{\text{modal}}(\hbar\omega) = \Gamma G^{\text{material}}(\hbar\omega). \quad (21)$$

The momentum matrix elements $|\langle i|\vec{a}\cdot\vec{p}|f\rangle(k',\phi)|^2$ depend on the wave number k' and the in-plane angle ϕ of the states i, f. They are calculated by multiplying the absolute squared overlap integral of the corresponding wave-function components with the momentum matrix element energy E_p, which can be looked up in Ref. 22, times $m_0/2$. One can identify the contributing valence-band wave-function components with the following rule:

$$\langle S|p_x|P_x\rangle = \langle S|p_y|P_y\rangle = P_\perp, \quad (22)$$

$$\langle S|p_z|P_z\rangle = P_\parallel, \quad (23)$$

with $|P_{\parallel/\perp}|^2 = E_{p\parallel/\perp}m_0/2$. All other combinations of momentum operator $p_{x,y,z}$ and basis state $|P_{x,y,z}\rangle$ vanish. For the choice of basis states made in Sec. III B, the matrix elements along the crystal directions are, for conduction-band spin-up states [see Eq. (11)]

$$\langle i|p_x|f\rangle = P_\perp(-\langle\psi_c|\psi_{v,1}\rangle + \langle\psi_c|\psi_{v,2}\rangle), \quad (24)$$

$$\langle i|p_y|f\rangle = P_\perp(i\langle\psi_c|\psi_{v,1}\rangle + i\langle\psi_c|\psi_{v,2}\rangle), \quad (25)$$

$$\langle i|p_z|f\rangle = P_\parallel\langle\psi_c|\psi_{v,3}\rangle, \quad (26)$$

and for conduction-band spin-down states

$$\langle i|p_x|f\rangle = P_\perp(\langle\psi_c|\psi_{v,4}\rangle - \langle\psi_c|\psi_{v,5}\rangle), \quad (27)$$

$$\langle i|p_y|f\rangle = P_\perp(i\langle\psi_c|\psi_{v,4}\rangle + i\langle\psi_c|\psi_{v,5}\rangle), \quad (28)$$

$$\langle i|p_z|f\rangle = P_\parallel\langle\psi_c|\psi_{v,6}\rangle, \quad (29)$$

with the componentwise overlap integral

$$\langle\psi_c|\psi_{v,j}\rangle = \int dz'\ \psi_c^*(z')\psi_{v,j}(z'), \quad (30)$$

where $\psi_{v,j}$ means the jth component of the (valence-band) wave function $\vec{\psi}_v$ of the final state $|f\rangle$ and ψ_c is the (conduction-band) wave function of the initial state $|i\rangle$. Again, the dependencies of the wave functions, and thus the overlap integrals, on the in-plane wave vector have been omitted to simplify the notation. The absolute squared matrix element for an arbitrary photon polarization vector $\vec{a}$ in the x-z plane ($\vec{a}=\sin\alpha\vec{e}_x+\cos\alpha\vec{e}_z$, where α is the angle to the c axis) can then be calculated (for a conduction-band spin-up state) as follows:

$$\begin{aligned}|\langle i|\vec{a}\cdot\vec{p}|f\rangle|^2 &= |\langle i|\sin\alpha p_x + \cos\alpha p_z|f\rangle|^2 = |\langle i|\sin\alpha p_x|f\rangle \\ &+ \langle i|\cos\alpha p_z|f\rangle|^2 = \sin^2\alpha|P_\perp|^2|\langle\psi_c|\psi_{v,1}\rangle \\ &- \langle\psi_c|\psi_{v,2}\rangle|^2 + \cos^2\alpha|P_\parallel|^2|\langle\psi_c|\psi_{v,3}\rangle|^2 \\ &- 2\sin\alpha\cos\alpha\Re[P_\perp P_\parallel^*\langle\psi_{v,3}|\psi_c\rangle\cdot(\langle\psi_c|\psi_{v,1}\rangle \\ &- \langle\psi_c|\psi_{v,2}\rangle)]. \end{aligned} \quad (31)$$

In order to calculate the transition matrix elements for the extraordinary and the ordinary modes of the semipolar waveguide, α is set to 0° or 90°, respectively. For the TM mode of the semipolar waveguide, we set $\alpha=-58°$, as this mode is not polarized parallel to a crystal direction but to the growth axis which corresponds to the z' direction, whereas for the TE mode the p_y-matrix element has to be used. Equation (31) shows that the absolute squared matrix element for a specific polarization direction, which enters the gain calculation, cannot be calculated out of the absolute squared matrix elements for other directions due to the last term on the right-hand side. Consequently, the gain spectrum for a specific polarization can generally not be calculated out of the gain spectra for other polarizations. In particular the gain on the extraordinary and ordinary modes is not just an intermediate value between TE and TM optical gain.

D. Self-consistent electric field

In order to determine the band structure and the wave functions in the quantum well, we need to know the electric potential $\Phi_p(z')$. InGaN/GaN heterostructures show both strain-induced and spontaneous polarization. The z' components of the polarizations for the quantum well and the barrier layer are[3]

$$\begin{aligned}P_{z'}^{(QW)} &= P_{sp}^{(QW)}\cos\theta + (2d_{15}c_{44}\epsilon_{xz})\sin\theta + \{[d_{31}(c_{11}+c_{12}) \\ &+ d_{33}c_{13}](\epsilon_{xx}+\epsilon_{yy}) + (2d_{31}c_{13}+d_{33}c_{33})\epsilon_{zz}\}\cos\theta, \end{aligned} \quad (32)$$

$$P_{z'}^{(b)} = P_{sp}^{(b)}\cos\theta. \quad (33)$$

Here, $P_{sp}^{(QW/b)}$ denote the spontaneous polarizations of the QW and the barrier layer and d_{ij} denote the piezoelectric constants. The spontaneous polarization for the quantum well is calculated using a bowing parameter for InGaN from Ref. 25. An electric field arises from the discontinuities of the polarization at the borders of the quantum well,

$$E_{z'} = \frac{P_{z'}^{(b)} - P_{z'}^{(QW)}}{\varepsilon\varepsilon_0}. \quad (34)$$

Here, ε is the material's static dielectric constant and ε_0 is the permittivity in vacuum. Figures 9(a) and 9(b) show the

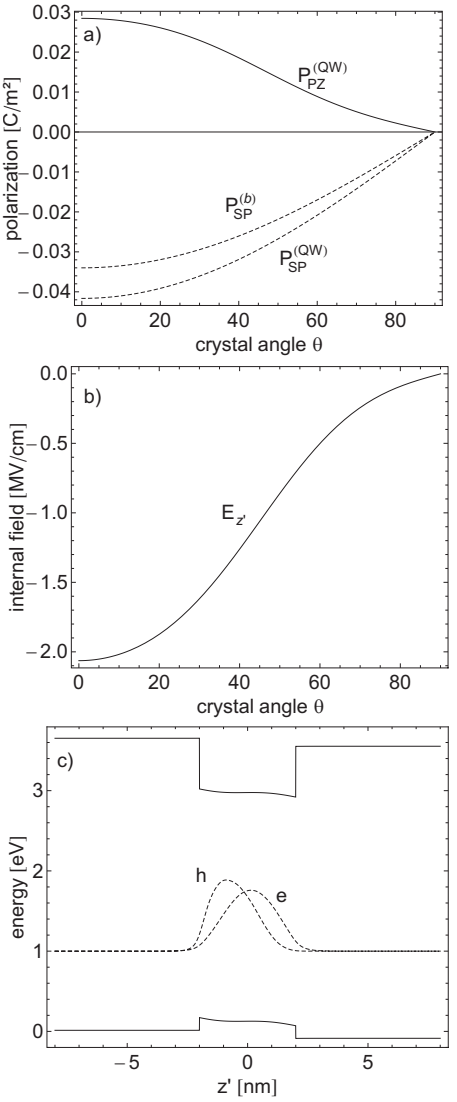

FIG. 9. (a) Piezoelectric polarization $P_{PZ}^{(QW)}$ and spontaneous polarizations $P_{SP}^{(b)}$, $P_{SP}^{(QW)}$ in the barrier and quantum well and (b) unscreened internal field $E_{z'}$ in the quantum well depending on the crystal angle θ and potential [(c), solid lines] with electron and hole probability distributions (dashed lines) for a 3 nm $In_{0.2}Ga_{0.8}N$ quantum well grown on the $(11\bar{2}2)$ plane at a sheet-carrier density of 2×10^{12} cm^{-2}.

components of the polarization and the electric field for a 3 nm $In_{0.2}Ga_{0.8}N$ quantum well depending on the crystal angle θ. Using the parameters from Ref. 22, we do not observe a zero in the electric field at an angle of about 58° like in other publications on this topic (see Ref. 21, for example). This finding is supported by a recent experimental study,[26] which also indicates that the electric field does not change sign at an angle between 0° and 90°. The internal field causes the quantum confined Stark effect, narrowing the band gap and drawing the electron and hole wave functions apart from each other [see Fig. 9(c)]. Thereby, the wave-function overlap and thus the optical matrix elements are reduced, resulting in a worse optical gain for devices that are affected by strong internal fields. However, simply inserting this electric field into the Schrödinger equations (9) and (10) gives wrong results. As stressed in Ref. 27, the screening of the electric field by the charge carriers has to be considered in light-emitting GaN/InGaN devices. We thus use the following self-consistent approach: the wave functions are calculated using the potential that arises from the polarization discontinuities and the resulting charge distribution is then included into an improved potential, which is then used to calculate the wave functions again. This calculation is repeated until the potential becomes stationary.

First, we set $\Phi_p(z')=eE_{z'}z'$ and determine the wave functions of the highest valence band and the lowest conduction band at the Γ point. Then we integrate the Poisson equation to get the electric potential that is caused by the charge-carrier distribution

$$\rho(z') = n_c e(|\vec{\psi}_v(z')|^2 - |\psi_c(z')|^2),$$

$$\Phi_\rho(z') = -\frac{1}{\varepsilon\varepsilon_0}\int_{-\infty}^{z'} d\zeta \int_{-\infty}^{\zeta} d\zeta' \rho(\zeta'), \tag{35}$$

where n_c is the two-dimensional charge-carrier density. Under-relaxation must be used to achieve convergence for high charge-carrier densities. The new potential is then

$$\Phi^{new} = \Phi^{old} + r\Phi_\rho \tag{36}$$

with the under-relaxation parameter $r \leq 1$. Here, we have made the approximation that only the wave functions at the Γ point are considered. In principle, we would have to calculate the wave functions for all considered bands depending on k_x' and k_y' and fill them according to the Fermi-Dirac distribution function, but this is numerically not practicable. However, the probability distribution of the electrons and holes does not change much with k_x', k_y', so considering only the Γ-point wave functions is a useful approximation.

E. Material gain

Having determined the band structure and the wave functions in the k_x', k_y' plane, we can calculate the material gain in the free-carrier picture with an *ad hoc* inclusion of the band-gap renormalization as follows:[23]

$$G^{(a)}(\hbar\omega) = \frac{e^2}{4\pi^2 c_0 \varepsilon_0 m_0^2 n_{eff} \omega E_\gamma d} \sum_{i,f} \int_0^\infty k' dk' \times \int_0^{2\pi} d\phi |\langle i|\vec{a}\cdot\vec{p}|f\rangle(k',\phi)|^2 [f_c(E_i(k',\phi)) - f_v(E_f(k',\phi))] \mathrm{sech}\left(\frac{\Delta E_{if}(k',\phi)-\hbar\omega}{E_\gamma}\right), \tag{37}$$

$$f_{c/v}(E) = \{1+\exp[(E-\mu_{c/v})/k_BT]\}^{-1}, \tag{38}$$

$$\Delta E_{if}(k',\phi) = E_i(k',\phi) - E_f(k',\phi). \tag{39}$$

The symbols appearing in this formula are the effective index of refraction n_{eff}, the vacuum speed of light c_0, the vacuum permittivity ε_0, the free-electron mass m_0, the quan-

tum well thickness d, the Boltzmann constant k_B, and the temperature $T=300$ K. The index a corresponds to the photon polarization vector $\vec{a}$ and i and f number the conduction and the valence bands, respectively (where spin-up and spin-down conduction-band electrons are treated as separate bands). $\vec{k}'=k'\cos\phi\vec{e}_{x'}+k'\sin\phi\vec{e}_{y'}$ is the electron or hole wave vector, which is integrated over the quantum well plane. Homogeneous broadening is incorporated by a sech function of width $E_\gamma=25$ meV.[28] The formulas in this section are adapted from Ref. 23, where we add the in-plane angle integration to account for the missing rotational symmetry and we use the momentum matrix element instead of the dipole matrix element, which are related via

$$|\langle\vec{a}\cdot\vec{r}\rangle|^2=\frac{\hbar^2}{m_0^2\Delta E_{if}(k',\phi)^2}|\langle\vec{a}\cdot\vec{p}\rangle|^2. \tag{40}$$

The quasi-Fermi energies μ_c, μ_v that enter the Fermi-Dirac functions are determined by the condition

$$n_c=\sum_i\frac{1}{(2\pi)^2}\int d^2k' f_c[E_i(k',\phi)]$$

$$=\sum_f\frac{1}{(2\pi)^2}\int d^2k' f_v[E_f(k',\phi)]. \tag{41}$$

Band-gap renormalization shifts the band gap by the Coulomb-hole self-energy ΔE_{CH} and the individual bands by the screened exchange $\Delta E_{SX,f/i}$, conduction bands downward and valence bands upward. These corrections are (in SI units)

$$\Delta E_{CH}=-2E_Ra_0\int_0^\infty dk'\frac{1}{1+\frac{k'}{\kappa}+\frac{Ca_0k'^3}{32\pi n_c}}, \tag{42}$$

$$\Delta E_{SX,i}=-\frac{E_Ra_0}{\pi\kappa}\int d^2k'\ \Theta(k')f_c(E_i(k',\phi)), \tag{43}$$

$$\Delta E_{SX,f}=-\frac{E_Ra_0}{\pi\kappa}\int d^2k'\Theta(k')[1-f_v(E_f(k',\phi))], \tag{44}$$

with

$$\Theta(k')=\frac{1+\frac{Ca_0\kappa k'^2}{32\pi n_c}}{1+\frac{k'}{\kappa}+\frac{Ca_0k'^3}{32\pi n_c}},$$

$$\kappa=\frac{e^2}{2\varepsilon\varepsilon_0}\left(\frac{dN_{2d,c}}{d\mu_c}-\frac{dN_{2d,v}}{d\mu_v}\right).$$

Here, E_R and a_0 are the exciton Rydberg energy and the Bohr radius and $N_{2d,c/v}(\mu_{c/v})$ is the conduction-band/valence-band charge-carrier density depending on the quasi-Fermi energy. At this level of simplification, the calculation includes a numerical parameter C to be chosen between 1 and 4.[23] It influences the width of the band gap on a range of several 10 meV. We used it as a fit parameter to reproduce gain peak positions for c-plane laser diodes from measurements[29] and found that $C=4$ works best for our simulations. The renormalized conduction- and valence-band energies that enter Eq. (39) are then

$$E_i^{(ren)}(k',\phi)=E_i^{(0)}(k',\phi)+\Delta E_{CH}+\Delta E_{SX,i}, \tag{45}$$

$$E_f^{(ren)}(k',\phi)=E_f^{(0)}(k',\phi)-\Delta E_{SX,f}. \tag{46}$$

F. Inhomogeneous broadening

Inhomogeneous broadening caused by spatial fluctuations in indium content and quantum well thickness is considered in a constant Fermi-energy model. It has already been pointed out in Ref. 29 that this model is more realistic than a convolution of the gain curve with a Gaussian function, which corresponds to a random distribution of quantum wells with different Fermi energies, as the carriers can move freely in the quantum well and compensate locally varying Fermi levels. We treat the effect of the indium fluctuations as fluctuations in the band-gap energy, where the quasi-Fermi levels are kept constant, and obtain the gain as an integral over gain curves with different band gaps weighted with a Gaussian distribution $\Omega(E',\sigma)$, where a broadening of $\sigma=60$ meV has been assumed, corresponding to an indium content fluctuation of $\Delta x=0.016$,

$$G_{\text{inh}}^{(a)}(\hbar\omega)=\int dE' G_{\Delta E\to\Delta E+E'}^{(a)}(\hbar\omega)\Omega(E',\sigma). \tag{47}$$

Here, $G_{\Delta E\to\Delta E+E'}^{(a)}$ is the material gain calculated from Eq. (39), where the band energies E_f and E_i are shifted such that the transition energy $\Delta E(k',\phi)$ becomes $\Delta E(k',\phi)+E'$. This step is equivalent to a convolution of the density of states with a Gaussian function as proposed in Ref. 29. The same broadening has to be applied to the integrals in Eq. (41) to obtain the correct quasi-Fermi levels.

IV. RESULTS AND DISCUSSION

We have calculated gain spectra of 3 nm $In_{0.2}Ga_{0.8}N$ quantum wells for c-plane, semipolar, and nonpolar crystal orientations and ridge geometries parallel and perpendicular to the projection of the c axis in the QW plane, as indicated in Fig. 1. The differences in the spectra are explained using the momentum matrix elements and the reduced densities of states for the various configurations. A variation of the crystal angle shows how the gain of the different modes evolves when going from the c plane to the a plane (or m plane).

A. Gain spectra

The material gain for the different crystal angles is calculated using Eq. (37). For the semipolar and the nonpolar planes it is important to distinguish between the two different ridge geometries: as stressed before, if the ridge points along the projection of the c axis on the QW plane [see Fig. 1(a)] then the eigenmodes of the ridge waveguide show TE and TM polarization. Gain spectra for these directions at various sheet-carrier densities are shown in Fig. 10. On the other

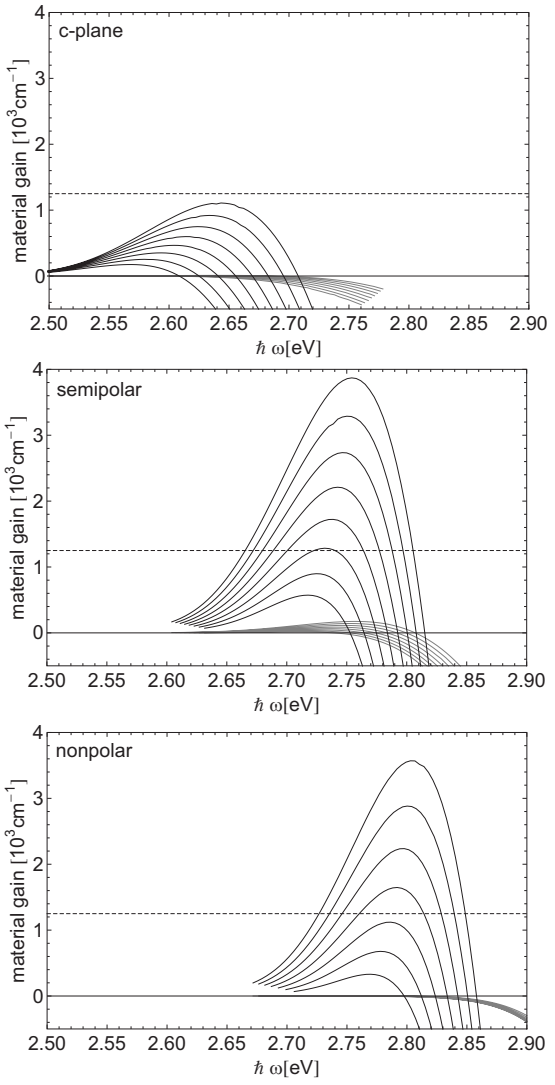

FIG. 10. Material gain for TE mode (black curves) and TM mode (gray curves) of *c* plane and semipolar and nonpolar quantum wells with ridge orientation parallel to the projection of the *c* axis on the QW plane. Estimated threshold gain is indicated as a dashed line. Sheet-carrier densities are (from bottom to top) 5×10^{12}–8.5×10^{12} cm^{-2} (*c* plane), 4×10^{12}–7.5×10^{12} cm^{-2} (semipolar), and 3×10^{12}–6×10^{12} cm^{-2} (nonpolar) in steps of 0.5×10^{12} cm^{-2}.

hand, if the ridge is oriented perpendicular to the *c* axis [see Fig. 1(b)] then the modes align to the extraordinary and ordinary directions of the birefringent crystal, which correspond to the [0001] and the $[11\bar{2}0]$ directions, respectively. Figure 11 shows gain spectra for these polarizations. Here, we want to point out that in our calculations there is no difference between the nonpolar *a* plane and *m* plane due to the symmetry properties of the utilized bulk Hamiltonian, so the results marked with "nonpolar" are valid for both crystal planes.

Assuming combined mirror and absorption losses of 25 cm^{-1} and a confinement factor of 0.02, one gets a threshold material gain of 1.25×10^{3} cm^{-1}, which is drawn as a dashed line in Figs. 10 and 11. The threshold sheet-carrier densities can then be estimated from the gain curves. They are 9.0×10^{12} cm^{-2} for *c*-plane, 5.3×10^{12} cm^{-2} for semipolar ($11\bar{2}2$), and 4.3×10^{12} cm^{-2} for nonpolar ($11\bar{2}0$) crystal orientation. One can thus expect a significant reduction in the threshold current density when employing semipolar or nonpolar quantum wells, although the reduced QCSE also increases the spontaneous emission and the Auger recombination rate and thus decreases the charge-carrier lifetime, so the changes in the threshold current will not be proportional to the changes in the carrier density.

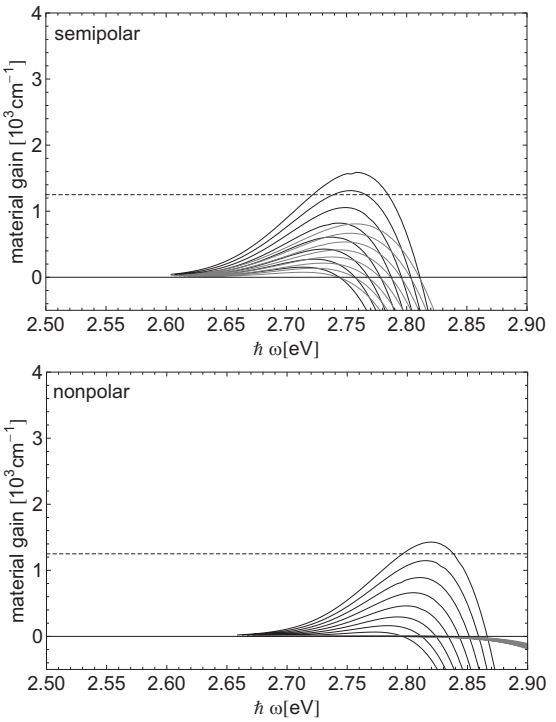

FIG. 11. Material gain for extraordinary mode (black curves) and ordinary mode (gray curves) of semipolar and nonpolar quantum wells with ridge orientation perpendicular to the *c* axis. Estimated threshold gain is indicated as a dashed line. Sheet-carrier densities are (from bottom to top) 4×10^{12}–7.5×10^{12} cm^{-2} (semipolar and nonpolar) in steps of 0.5×10^{12} cm^{-2}.

As mentioned before, the rotational symmetry in the QW plane is lost when going from the *c* plane to a semipolar or nonpolar quantum well, so the orientation of the ridge relative to the *c* axis affects the modes of the waveguide and thus the optical gain. The modes in a ridge waveguide oriented perpendicular to the *c* axis (see Fig. 11) show a worse gain than the TE mode of the other orientation (see Fig. 10), especially for the nonpolar case. For the semipolar quantum well, one gets a positive gain on both the ordinary and the extraordinary modes, but it is less than half of the TE-gain value. Lasing on these modes should in principle be possible, as the threshold carrier densities are still lower than the one for the *c*-plane TE mode. However, the other ridge orientation offers substantially higher gain and thereby lower threshold charge-carrier densities. Ridge laser diodes on semipolar or nonpolar crystal planes should thus be oriented along the projection of the *c* axis on the quantum well plane. In the semipolar ($11\bar{2}2$) case this means that the ridge waveguide should point along the $[\bar{1}\bar{1}23]$ direction with laser facets formed by etching.

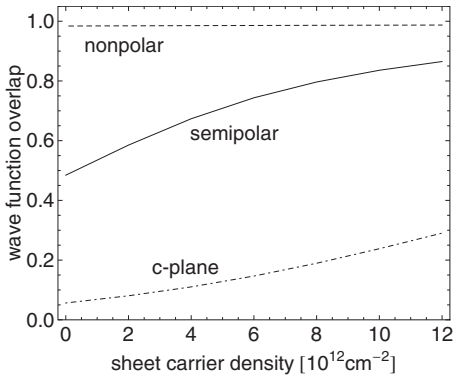

FIG. 12. Absolute squared electron $e1$ and hole $A1$ wave-function overlap at the Γ point as a function of charge-carrier density for c plane, semipolar $(11\bar{2}2)$, and nonpolar $(11\bar{2}0)$ quantum wells.

The results presented here are in agreement with experiments on semipolar and nonpolar structures: direction-dependent stimulated emission measurements have been published for quantum well structures on semipolar[4] and nonpolar substrates.[30] Both experiments showed that the stimulated emission for photon propagation along the projection of the c axis is significantly higher than for propagation perpendicular to the c axis, matching our findings that modes with a polarization perpendicular to the c axis have the highest gain.

B. Momentum matrix elements

The main reason why semipolar and nonpolar quantum wells show much higher gain for a given sheet-carrier density than c-plane ones is the reduction in the quantum confined Stark effect. As can be seen from Fig. 12, the wave-function overlap $\Sigma_{i=1}^{6}|\langle\psi_c|\psi_{v,i}\rangle|^2$ in a c-plane quantum well is drastically reduced by the QCSE. Although the internal field is partially screened by the charge carriers, the overlap does not exceed 0.3 for realistic charge-carrier densities. On the other hand, the overlap ranges between 0.5 and 0.8 for the semipolar quantum well, where the internal field is reduced by the crystal orientation and for the nonpolar quantum well it is almost 1, as the internal field perpendicular to the quantum well plane vanishes completely in that case. The wave-function overlap directly affects the momentum matrix elements [see Eqs. (26) and (29)] which enter the gain calculation. One also has to consider the effects of quantum confinement and biaxial strain in the valence-band Hamiltonian, which depend on the crystal angle. They affect the composition of the valence-band wave functions and thus the componentwise overlap, so the matrix elements for different polarization directions change with the crystal angle. Figures 13 and 14 show the momentum matrix elements of the lowest-energy transitions $e1$-$A1$ and $e1$-$B1$ averaged over the in-plane angle ϕ for the TE and TM modes and the ordinary and extraordinary modes, respectively. From the matrix elements one can see why certain modes have high gain while others have less or none. Important for the gain is a high matrix element for low-energy transitions in the vicinity of

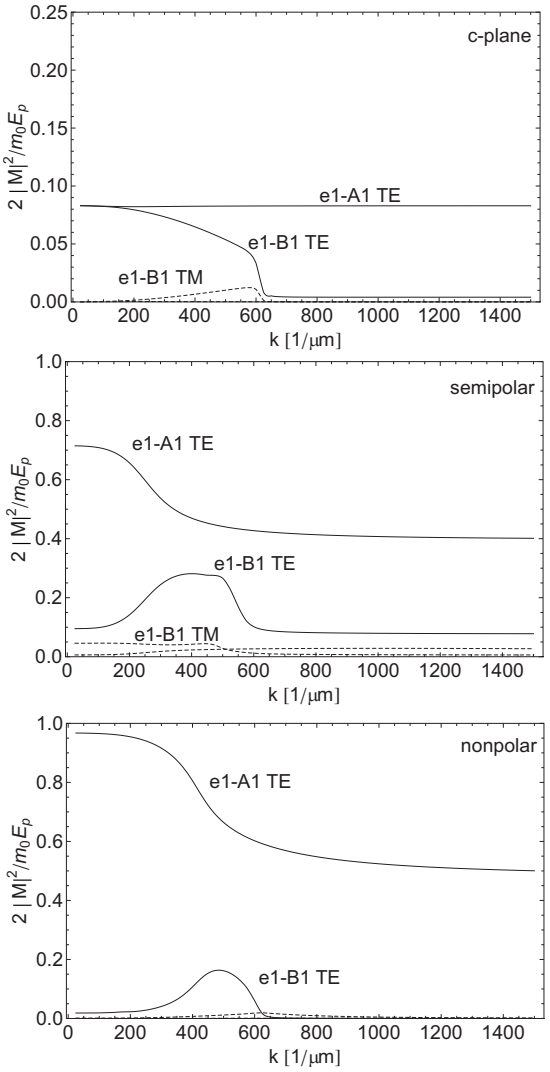

FIG. 13. In-plane averaged absolute squared momentum matrix elements of the two lowest-energy transitions for TE mode (solid curves) and TM mode (dashed curves) as a function of the wave number for different quantum well orientations (matrix elements not drawn are essentially zero). Note the different scales for c plane and semipolar and nonpolar. The sheet-carrier density is 7×10^{12} cm^{-2}.

the Γ point $(k=0)$, as this is where the inversion condition

$$\mu_c - \mu_v > E_i(k',\phi) - E_f(k',\phi) > E_g \tag{48}$$

is fulfilled at realistic charge-carrier densities. As expected from the wave-function overlap, the matrix elements for the c plane are much smaller than for semipolar or nonpolar planes, which explains why the non-c-plane structures exhibit much higher gain at a given charge-carrier density. The TM-matrix elements are close to zero for the topmost transitions in all structures and therefore the TM modes do not show any significant gain at the considered charge-carrier densities. Furthermore, it becomes clear why the extraordinary and the ordinary modes have lower gain than the TE modes: they do have nonvanishing matrix elements, but

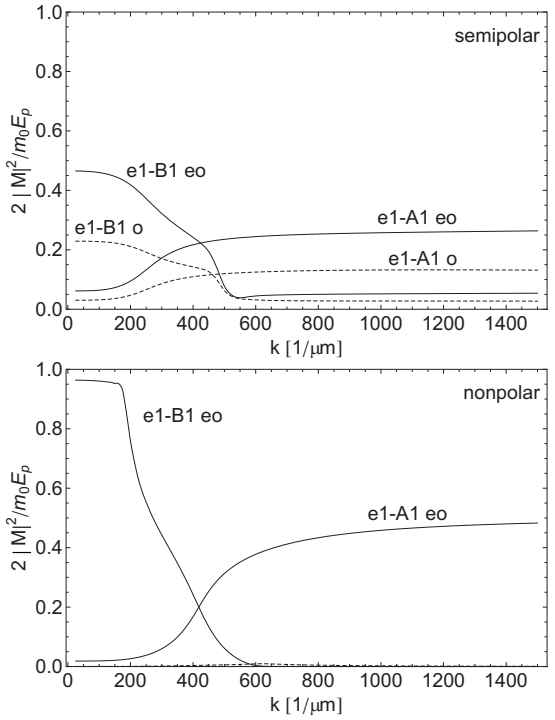

FIG. 14. In-plane averaged absolute squared momentum matrix elements of the two lowest-energy transitions as a function of the wave number for ordinary (dashed curves) and extraordinary (solid curves) modes for different quantum well orientations (matrix elements not drawn are essentially zero). The sheet-carrier density is 7×10^{12} cm^{-2}.

these correspond to the $e1$-$B1$ transition, which has higher energy than $e1$-$A1$ and thus less inversion.

C. Reduced density of states

Comparing the gain spectra for nonpolar and semipolar quantum wells, it still remains to be explained why the TE gain for the nonpolar structure is almost twice as high at a given charge-carrier density, and why the gain on the extraordinary mode is so much lower although there is a high matrix element for this mode (see fig. 14). Therefore, one has to look at the reduced density of states

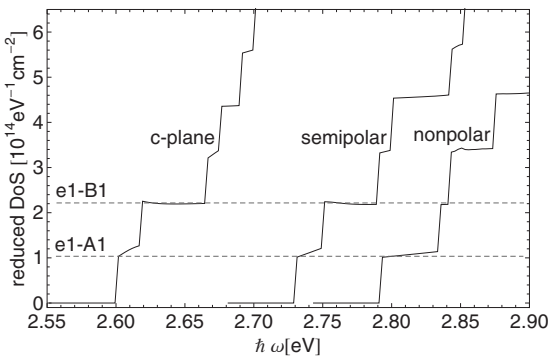

FIG. 15. Reduced density of states for different crystal orientations at a sheet-carrier density of 7×10^{12} cm^{-2}.

$$d(\hbar\omega)=\frac{1}{(2\pi)^2}\sum_{i,f}\int d^2k'\,\delta(\Delta E(k',\phi)-\hbar\omega). \quad (49)$$

For non-c-plane quantum wells $d(\hbar\omega)$ does not directly enter the gain formula, as matrix elements and energies depend on the in-plane angle ϕ, so the integral over the in-plane wave vector cannot be converted into an integral over the energy. However, it is still useful to look at the reduced density of states, as one can see the different possible transitions and how they contribute to the inversion. Figure 15 shows results for $d(\hbar\omega)$ for the different crystal orientations.

While $d(\hbar\omega)$ does not change a lot in shape from the c plane to the semipolar plane except for a shift to higher energies due to the reduced QCSE, the reduced density of states for the nonpolar plane shows one important difference: the $e1$-$B1$ transition is shifted away from the $e1$-$A1$ transition, so $e1$-$A1$ has more inversion at low charge-carrier densities than in the semipolar case. This considerably improves the TE gain, as the $e1$-$A1$ transition contributes mainly to the TE-matrix element at the Γ point (see Fig. 13). On the other hand, achieving inversion on the $e1$-$B1$ transition, which is responsible for the gain on the extraordinary mode, becomes possible only at high charge-carrier densities, as there are many states below the $e1$-$B1$ energy gap. The gain on the extraordinary mode is thus blueshifted and much weaker than the TE gain.

D. Variation of the crystal angle

It has been shown in the preceding sections that the gain on the optical eigenmodes depends strongly on the crystal angle, which influences the magnitude of the QCSE, the wave-function overlap, the strain shifts in the Hamiltonian, and the polarization of the modes. In order to investigate the transition from c plane to nonpolar, we vary the crystal angle in our calculation at a fixed charge-carrier density. The resulting gain spectra are depicted in Fig. 16. As a consequence of the reduced QCSE, the TE-gain peak increases and shifts to blue with increasing angle, whereas the TM gain stays close to zero due to the vanishing matrix elements of the relevant transitions for any crystal angle. The reduction in the QCSE in combination with the changes in the density of states improves the gain by a factor of about 10 when going from the c plane to the a plane at $n_c=7\times10^{12}$ cm^{-2}. For the semipolar orientation, the improvement is smaller, about a factor of 5 with respect to the c-plane, but the laser wavelength for a given indium content is higher, which might be desirable for realizing green laser diodes.

If the ridge is oriented perpendicular to the c axis, the situation is more complicated: for $\theta=0$ (c plane), the extraordinary and the ordinary directions correspond to the TM and the TE modes, respectively. This is reversed when going to $\theta=90°$. The gain on the ordinary mode thus rises first at small angles due to the reduced QCSE, but then falls with increasing angle as the mode is rotated toward the TM orientation. The extraordinary mode is rotated away from the TM orientation, so its gain also rises at small angles, but it goes down again at higher angles due to the changes in the reduced density of states mentioned above. Both modes have

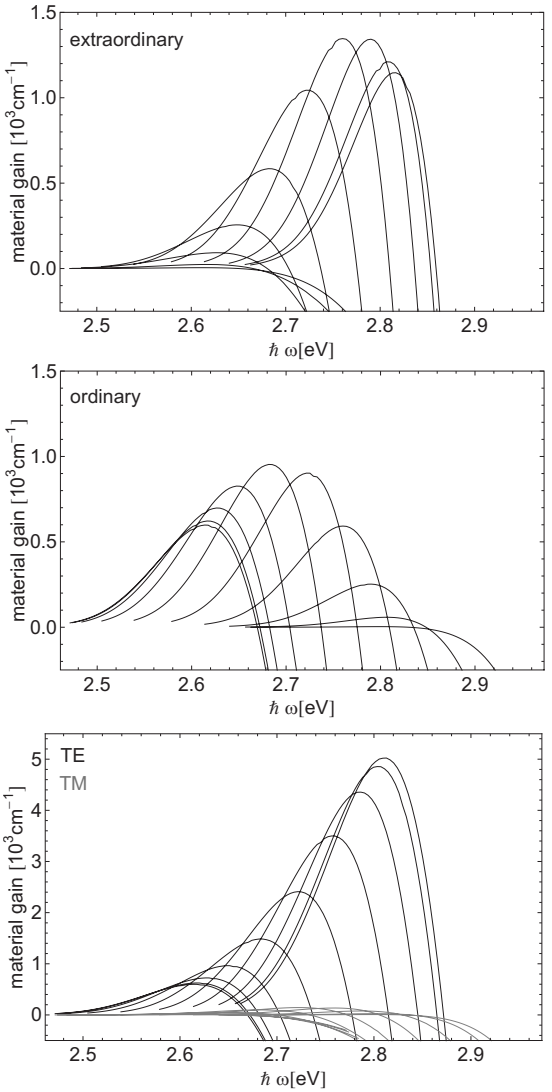

FIG. 16. Gain spectra for different crystal angles θ and ridge orientation perpendicular (top and middle) and parallel (bottom) to the projection of the c axis in the QW plane at a charge-carrier density of 7×10^{12} cm^{-2}. The angle is varied from 0° (c plane) to 90° (a plane) in steps of 10°, from left to right (note the different scales).

lower gain than the TE mode of the other ridge orientation for any crystal angle, so non-c-plane laser diodes with ridges perpendicular to the c axis should generally perform worse than those with the other ridge orientation.

V. CONCLUSION

To sum up, we present a method to calculate the optical gain in the free-carrier picture with an *ad hoc* inclusion of the band-gap renormalization for semipolar and nonpolar InGaN quantum wells. The eigenmodes and their polarizations are determined for the birefringent waveguide, and it is shown that they have to be considered in the orientation of the momentum matrix elements. Gain spectra are calculated for semipolar $(11\bar{2}2)$ and nonpolar $(11\bar{2}0)$ planes for different charge-carrier densities and compared to the c-plane case, examining also the two different ridge orientations that can be realized in non-c-plane structures. It is found that the TE-mode gain for a ridge orientation parallel to the projection of the c axis on the quantum well plane can be greatly increased when going from the c-plane to a nonpolar orientation and therefore we recommend this ridge orientation for semipolar and nonpolar laser diodes. On the other hand, the extraordinary and the ordinary modes for the other ridge geometry did not show great improvement for any crystal orientation. The behavior of the different modes is explained by changes in the band structure and the reduction in the quantum confined Stark effect, which leads to an increase in the electron and hole wave-function overlap and thus of the momentum matrix elements. From these results we can conclude that semipolar and nonpolar quantum wells offer great possibilities for laser diode structures with higher indium content, where lasing from c-plane quantum wells is suppressed by the QCSE.

ACKNOWLEDGMENTS

The authors acknowledge funding by Deutsche Forschungsgemeinschaft (DFG) within the research group 957, PolarCon.

APPENDIX A: 4×4 TRANSFER-MATRIX METHOD

The 4×4 transfer-matrix method[14,31] calculates the wave front in an anisotropic planar layer waveguide for a wave that propagates in the y direction; the layers are perpendicular to the z direction (in this description, unprimed coordinates are used for the waveguide to simplify the notation; they correspond to the primed coordinates in Secs. II A and III). For this method it is necessary to assume that the electric and the magnetic fields do not depend on the x coordinate, which is true for a wave propagating in the y direction in an infinite film. This simplification is justified if the lateral extensions of the planar waveguide are much bigger than the transversal ones. The Maxwell equations for such a structure are

$$\nabla\cdot(\varepsilon\vec{E})=0,$$

$$\nabla\cdot\vec{B}=0,$$

$$\nabla\times\vec{E}=i\omega\vec{B},$$

$$\nabla\times\vec{B}=-i\frac{\omega}{c_0^2}\varepsilon\vec{E}. \tag{A1}$$

Here, time derivatives have been replaced with $-i\omega$, ε is the nondiagonal dielectric tensor (with components ε_{ij}) that depends on z, and c_0 is the speed of light in vacuum. The wave propagates in the y direction, so the y dependence is simply $\exp(iyn_{\mathrm{eff}}\omega/c_0)$ and all y derivatives are replaced with $in_{\mathrm{eff}}\omega/c_0$, where n_{eff} is an effective index of refraction which describes the propagation in the whole structure. This effective index is to be determined by the calculation. Rearrang-

ing the last two equations in Eq. (A1) gives for the components of the fields

$$\frac{d}{dz}\begin{pmatrix} E_y \\ c_0 B_x \\ E_x \\ c_0 B_y \end{pmatrix} = i\frac{\omega}{c_0}\Delta\begin{pmatrix} E_y \\ c_0 B_x \\ E_x \\ c_0 B_y \end{pmatrix}, \tag{A2}$$

$$c_0 B_z = n_{\text{eff}} E_x, \tag{A3}$$

$$E_z = -\frac{\varepsilon_{zy}}{\varepsilon_{zz}}E_y - \frac{\varepsilon_{zx}}{\varepsilon_{zz}}E_x - \frac{n_{\text{eff}} c_0}{\varepsilon_{zz}}B_x, \tag{A4}$$

$$\Delta = \begin{pmatrix} -n_{\text{eff}}\frac{\varepsilon_{zy}}{\varepsilon_{zz}} & 1-\frac{n_{\text{eff}}^2}{\varepsilon_{zz}} & -n_{\text{eff}}\frac{\varepsilon_{zx}}{\varepsilon_{zz}} & 0 \\ \varepsilon_{yy}-\frac{\varepsilon_{yz}\varepsilon_{zy}}{\varepsilon_{zz}} & -n_{\text{eff}}\frac{\varepsilon_{yz}}{\varepsilon_{zz}} & \varepsilon_{yx}-\frac{\varepsilon_{yz}\varepsilon_{zx}}{\varepsilon_{zz}} & 0 \\ 0 & 0 & 0 & -1 \\ -\varepsilon_{xy}+\frac{\varepsilon_{xz}\varepsilon_{zy}}{\varepsilon_{zz}} & n_{\text{eff}}\frac{\varepsilon_{xz}}{\varepsilon_{zz}} & n_{\text{eff}}^2-\varepsilon_{xx}+\frac{\varepsilon_{xz}\varepsilon_{zx}}{\varepsilon_{zz}} & 0 \end{pmatrix}. \tag{A5}$$

Formal integration of the first line in Eq. (A4) leads to

$$\vec{\phi}(z_{j+1}) = \exp[i\omega(z_{j+1}-z_j)\Delta]\vec{\phi}(z_j) =: T_L(z_{j+1}-z_j)\vec{\phi}(z_j), \tag{A6}$$

$$\vec{\phi} = \begin{pmatrix} E_y \\ c_0 B_x \\ E_x \\ c_0 B_y \end{pmatrix}. \tag{A7}$$

Here, T_L is the transfer matrix for one layer. Multiplying the transfer matrices for all layers gives the T matrix, which connects the bottom and the top of the structure. For a guided mode, all fields must vanish for $z \to \pm\infty$. Assuming that the outside of the structure is vacuum, the matrix Δ for the outside takes the simple form

$$\Delta = \begin{pmatrix} 0 & 1-n_{\text{eff}}^2 & 0 & 0 \\ 1 & 0 & 0 & 0 \\ 0 & 0 & 0 & -1 \\ 0 & 0 & n_{\text{eff}}^2-1 & 0 \end{pmatrix}. \tag{A8}$$

This matrix has two twice degenerate eigenvalues $\pm i\beta$ with $\beta=\sqrt{1-n_{\text{eff}}^2}$. There are thus two $\vec{\phi}$ vectors that rise exponentially for $z\to\infty$ and decay for $z\to-\infty$, and two others that behave vice versa. The waveguiding condition now states that a guided mode must consist only of vectors that decay exponentially on the outside of the structure. An eigenvector to $-i\beta$ on the bottom should thus become an eigenvector to $+i\beta$ when propagated through the structure with the T matrix, which gives the equation

$$T\underbrace{\left[a\begin{pmatrix}0\\0\\i\\-\beta\end{pmatrix}+b\begin{pmatrix}\beta\\i\\0\\0\end{pmatrix}\right]}_{\text{eigenvectors to } -i\beta \text{ in vacuum}} = \underbrace{c\begin{pmatrix}0\\0\\i\\\beta\end{pmatrix}+d\begin{pmatrix}-\beta\\i\\0\\0\end{pmatrix}}_{\text{eigenvectors to } i\beta \text{ in vacuum}}. \tag{A9}$$

This is a homogeneous linear equation system for the coefficients a,b,c,d. A nonzero solution exists if the determinant vanishes. The waveguiding condition in its explicit form is then

$$\begin{aligned}&[T_{43}+i\beta(T_{44}+T_{33})-\beta^2 T_{34}][-T_{12}+i\beta(T_{11}+T_{22})+\beta^2 T_{21}] \\ &+[T_{42}+i\beta(T_{32}-T_{41})+\beta^2 T_{31}][T_{13}+i\beta(T_{14}-T_{23}) \\ &+\beta^2 T_{24}]=0.\end{aligned} \tag{A10}$$

T_{ij} are functions of n_{eff}, so Eq. (A10) allows the calculation of n_{eff} such that a guided mode is possible. This is done numerically. The highest n_{eff} that fulfils Eq. (A10) gives the fundamental mode of the waveguide structure.

Eigenmodes can now be calculated by inserting the so found n_{eff} into the matrix Δ and propagating the four vectors through the structure using Eq. (A7). The correct starting condition, the coefficients a and b, can be obtained from Eq. (A9), and the z components are given by Eq. (A4).

APPENDIX B: FOURIER SERIES EXPANSION OF THE HOLE EIGENFUNCTIONS

Wave equations like Eq. (9) can be solved numerically by expanding the eigenfunctions as finite Fourier series and thereby transforming the problem to a matrix eigenvalue equation. To do so, one has to impose periodic boundary conditions on a reference length L along the z' direction. The choice of this length affects the basis functions of the expansion, and it is useful to choose a multiple of the quantum well thickness, for example $L=4d$, which is used in our calculation. We use the following ansatz for the eigenfunctions:

$$\vec{\psi}(z') = \sum_{n=0}^{N}\frac{1}{\sqrt{L}}\vec{c}_n \exp(iq_n z') \tag{B1}$$

with $q_n=\frac{\pi}{L}(N-2n)$. N is the number of basis functions in which to expand and it has to be even to include $q=0$. These eigenfunctions are exact only in the limit $N\to\infty$, but it is found that for the ground state and the lower excited states the solutions converge rapidly and acceptable accuracy can already be achieved with $N=50$. Plane waves have been chosen as basis functions because they reduce the matrix operator $\mathbf{H_v}(k_x',k_y',k_z'=-i\frac{d}{dz'})$ to the bulk Hamiltonian $\mathbf{H_v}(k_x',k_y',q_n)$. Inserting this ansatz into Eq. (9), multiplying by $\frac{1}{\sqrt{L}}\exp(-iq_m z')$, and integrating over L gives

$$\{[\mathbf{H_v}(k_x',k_y',q_n)]_{ij}\delta_{mn}+V_{mn}\delta_{ij}\}(c_n)_j = E(c_m)_i, \tag{B2}$$

where δ_{mn},δ_{ij} are the Kronecker δ and V_{mn} is the Fourier transformation of the two potential terms: $V_{mn}=\frac{1}{L}\int_{-L/2}^{L/2}dz'\exp[-i(q_m-q_n)z'][V_{QW,v}(z')+\Phi_p(z')]$. Sum convention is used here and $i,j=1-6$ number the components of

the vectors $\vec{c}_n$ and $\vec{c}_m$, whereas $n,m=1$ to N number the basis functions of the Fourier expansion (B1). To treat this problem numerically, the indices j,n and i,m are transformed to one index via

$$\alpha = 6n + j, \quad \alpha' = 6m + i, \tag{B3}$$

where α,α' now go from 0 to $6(N+1)$. With this transformation, Eq. (B2) becomes a simple matrix eigenvalue equation

$$\mathcal{H}_{\alpha\alpha'} c_{\alpha'} = E c_\alpha \tag{B4}$$

with $\mathcal{H}_{(6n+j),(6m+i)} = [\mathbf{H_v}(k_x', k_y', q_n)]_{ij}\delta_{mn} + V_{mn}\delta_{ij}$. This equation can be solved numerically with any standard diagonalization algorithm, yielding both the energy eigenvalues and the corresponding eigenfunctions for k_x', k_y' as vectors with $6N$ components, which can be decomposed into the wave function's Fourier coefficient vectors $\vec{c}_n$ by inverting the index transformation (B3). This method is also applicable for the conduction-band Schrödinger equation, simplified by the fact that its eigenfunctions are scalar, so an index transformation like Eq. (B3) is not necessary.

*ulrich.schwarz@iaf.fraunhofer.de

[1] D. Queren, A. Avramescu, G. Brüderl, A. Breidenassel, M. Schillgalies, S. Lutgen, and U. Strauß, Appl. Phys. Lett. **94**, 081119 (2009).

[2] J. Seo Im, H. Kollmer, J. Off, A. Sohmer, F. Scholz, and A. Hangleiter, Phys. Rev. B **57**, R9435 (1998).

[3] S.-H. Park and S.-L. Chuang, Phys. Rev. B **59**, 4725 (1999).

[4] K. Kojima, M. Funato, Y. Kawakami, S. Masui, S. Nagahama, and T. Mukai, Appl. Phys. Lett. **91**, 251107 (2007).

[5] A. Tyagi, Y.-D. Lin, D. A. Cohen, M. Saito, K. Fujito, J. S. Speck, S. P. DenBaars, and S. Nakamura, Appl. Phys. Express **1**, 091103 (2008).

[6] A. Tyagi, H. Zhong, R. B. Chung, D. F. Feezell, M. Saito, K. Fujito, J. S. Speck, S. P. DenBaars, and S. Nakamura, Phys. Status Solidi C **5**, 2108 (2008).

[7] K. Okamoto, T. Tanaka, and M. Kubota, Appl. Phys. Express **1**, 072201 (2008).

[8] D. F. Feezell, M. C. Schmidt, R. M. Farrell, K.-C. Kim, M. Saito, K. Fujito, D. A. Cohen, J. S. Speck, S. P. DenBaars, and S. Nakamura, Jpn. J. Appl. Phys., Part 2 **46**, L284 (2007).

[9] K. Okamoto, J. Kashiwagi, T. Tanaka, and M. Kubota, Appl. Phys. Lett. **94**, 071105 (2009).

[10] Y. Enya, Y. Yoshizumi, T. Kyono, K. Akita, M. Ueno, M. Adachi, T. Sumitomo, S. Tokuyama, T. Ikegami, K. Katayama, and T. Nakamura, Appl. Phys. Express **2**, 082101 (2009).

[11] K. Kojima, H. Kamon, M. Funato, and Y. Kawakami, Jpn. J. Appl. Phys. **48**, 080201 (2009).

[12] K. Kojima, H. Kamon, M. Funato, and Y. Kawakami, Phys. Status Solidi C **5**, 3038 (2008).

[13] S. Shokhovets, R. Goldhahn, G. Gobsch, S. Piekh, R. Lantier, A. Rizzi, V. Lebedev, and W. Richter, J. Appl. Phys. **94**, 307 (2003).

[14] R. Wirth, A. Moritz, C. Geng, F. Scholz, and A. Hangleiter, Phys. Rev. B **55**, 1730 (1997).

[15] E. Kapon, Z. Rav-Noy, L. T. Lu, M. Yi, S. Margalit, and A. Yariv, Appl. Phys. Lett. **45**, 1159 (1984).

[16] G. Yu, H. Ishikawa, T. Egawa, T. Soga, J. Watanabe, T. Jimbo, and M. Umeno, Jpn. J. Appl. Phys., Part 2 **36**, L1029 (1997).

[17] N. A. Sanford, L. H. Robins, A. V. Davydov, A. Shapiro, D. V. Tsvetkov, A. V. Dmitriev, S. Keller, U. K. Mishra, and S. P. DenBaars, J. Appl. Phys. **94**, 2980 (2003).

[18] N. A. Sanford, A. Munkholm, M. R. Krames, A. Shapiro, I. Levin, A. V. Davydov, S. Sayan, L. S. Wielunski, and T. E. Madey, Phys. Status Solidi C **2**, 2783 (2005).

[19] R. Goldhahn, C. Buchheim, P. Schley, A. T. Winzer, and H. Wenzel, in *Nitride Semiconductor Devices: Principles and Simulations*, edited by J. Piprek (Wiley VCH, New York, 2007).

[20] A. Moritz, R. Wirth, C. Geng, F. Scholz, and A. Hangleiter, Appl. Phys. Lett. **68**, 1217 (1996).

[21] S.-H. Park, J. Appl. Phys. **91**, 9904 (2002).

[22] I. Vurgaftman and J. R. Meyer, in *Nitride Semiconductor Devices: Principles and Simulations*, edited by J. Piprek (Wiley VCH, New York, 2007).

[23] W. W. Chow and S. W. Koch, *Semiconductor-Laser Fundamentals* (Springer, Berlin, 1998).

[24] P. D. C. King, T. D. Veal, C. E. Kendrick, L. R. Bailey, S. M. Durbin, and C. F. McConville, Phys. Rev. B **78**, 033308 (2008).

[25] F. Bernardini and V. Fiorentini, Phys. Status Solidi A **190**, 65 (2002).

[26] M. Feneberg, F. Lipski, R. Sauer, K. Thonke, T. Wunderer, B. Neubert, P. Brückner, and F. Scholz, Appl. Phys. Lett. **89**, 242112 (2006).

[27] V. Ranjan, G. Allan, C. Priester, and C. Delerue, Phys. Rev. B **68**, 115305 (2003).

[28] B. Witzigmann, V. Laino, M. Luisier, U. T. Schwarz, H. Fischer, G. Feicht, W. Wegscheider, C. Rumbolz, A. Lell, and V. Härle, IEEE Photonics Technol. Lett. **18**, 1600 (2006).

[29] K. Kojima, U. T. Schwarz, M. Funato, Y. Kawakami, S. Nagahama, and T. Mukai, Opt. Express **15**, 7730 (2007).

[30] T. Onuma, K. Okamoto, H. Ohta, and S. F. Chichibu, Appl. Phys. Lett. **93**, 091112 (2008).

[31] M. Vassell, J. Opt. Soc. Am. **64**, 166 (1974).